Additively Manufactured Binder-Free Electrodes for Supercapacitors

Johannes Heumann,* Dominik Müller, Norman T. M. Baltes, Sebastian Geiger, Peter Schultz, Angelos Polyzoidis, and Jens Tübke

Energy storage systems are of immense importance for energy transition. For a successful process, it is very important that energy storage technologies used are as environmentally friendly as possible. The electrodes of batteries and supercapacitors are produced by coating a slurry onto metal foils. To ensure that the active material adheres to the metal foil, fluorinated binders such as polyvinylidene difluoride (PVDF) and polytetrafluorethylene (PTFE) are necessary, which belong to the per- and polyfluoroalkyl substances (PFAS) and are considered to be harmful to the environment. This study presents a new process for electrode production, using additive manufacturing, to overcome these problems. Complete electrodes are printed from a single piece, eliminating the need for metal foil and binders. Masked stereolithography method guarantees a high resolution of the structure and a fast production time. The printed nonconductive polymer electrodes are converted into porous polymer electrodes after a pyrolysis and activation step. Gas adsorption measurements provide a sufficient high specific surface area of 499 m^2 g^{-1} and a pore size distribution in the microporous range. Electrochemical experiments reveal that the printed electrodes are suitable for supercapacitor applications and are comparable to conventionally produced electrodes, especially for low current densities.

1. Introduction

Due to the energy transition, electrochemical energy storage systems are very popular these days.[1–3] Rechargeable batteries in particular dominate the market for electrochemical storage devices.[4–7] However, batteries also have disadvantages in terms of lifetime, power density, charging time, and critical raw materials.[8,9] These disadvantages are partially overcome by electrochemical capacitors, also known as supercapacitors. Supercapacitors are characterized especially by short charging/discharging times (seconds or minutes), a long lifetime, and an extremely high power density.[10–13] The manufacturing process for the respective electrodes is similar for both energy storage technologies. The required materials (active material, conductive additive, and binder) are dispersed in a solvent to form a slurry and subsequently coated onto a metal foil fixing the electrode and serving as a current collector.[14,15] The elimination of two components (binder and metal foil) could make the electrodes significantly more environmentally friendly and cost-efficient. The binders used, mostly PTFE and PVDF, pose an environmental risk as they belong to the PFAS group.[16–18] Furthermore, these polymers are not conductive and therefore contribute to higher resistance and poorer performance of the energy storage systems.[17,19] In addition, the use of metal foils as current collectors for aqueous systems has some additional disadvantages like weak adhesion of the active material, increased weight of the cell followed by decreased specific energy density, corrosion of metals by aqueous electrolytes, and high costs.[20–22]

Recently, new manufacturing processes enable to save on binder and metal foil for electrodes. Electrode production is now set to be revolutionized in combination with optical 3D printing methods.[23–25] The resinous starting material is polymerized layer by layer through targeted exposure. This successively produces high-precision, isotropic, geometrically freely configurable 3D blanks.[26,27] The nonconductive polymer is converted into an electrically conductive carbon structure by pyrolysis. This is associated with a loss of mass and shrinkage of the 3D structure. Residuals like oils, midvolatile compounds, short-chain gas compounds can be emitted.[28] Due to the requirements for electrode materials for batteries and supercapacitors differ, the following study will focus on supercapacitors, because of the high costs of suitable current collectors and electrode materials as well as their low energy density preventing commercialization.[20,29] The requirements for the electrode and the active material are diverse. A high specific surface area (SSA) and a pore size distribution of the active material in the range of both micropores (<2 nm) and mesopores (2–50 nm) are desirable. In addition, high electrical conductivity, chemical

J. Heumann, D. Müller, N. T. M. Baltes, S. Geiger, J. Tübke
Applied Electrochemistry Department
Fraunhofer Institute for Chemical Technology
Joseph-von-Fraunhofer-Straße 7, 76327 Pfinztal, Germany
E-mail: johannes.heumann@ict.fraunhofer.de

P. Schultz, A. Polyzoidis
Energetic Materials Department
Fraunhofer Institute for Chemical Technology
Joseph-von-Fraunhofer-Straße 7, 76327 Pfinztal, Germany

Batteries & Supercaps

Research Article
doi.org/10.1002/batt.202400455

Chemistry Europe
European Chemical
Societies Publishing

resistance, and good processability are preferred properties of active materials for supercapacitors.[30–33]

Optimizing the electrode materials remains a major challenge. Adjusting the proper porosity and conductivity has a significant influence on the energy and power density.[34] Carbon materials such as activated carbon, carbon nanotubes, and graphene are some of the commonly used active materials in supercapacitors.[35,36] These materials are available in the market, have good electrical conductivity, and can be purchased in basic forms. These basic forms reveal certain fixed properties (i.e., pore size or SSA, etc.) which cannot be tailored to respective supercapacitor applications.

Additionally, a free geometric definition of the produced electrodes is limited by the possible processing methods (e.g., casting, laser structuring, etc.).

Likewise, 3D-printed polymer structures produced with specialized resin formulations enable fine control of important material parameters. A subsequent pyrolysis step enables the conversion into electrically conductive carbon structures. Various analytical methods such as thermogravimetric analysis (TGA), mass spectrometry (MS),[37] pyrolysis gas chromatography with mass spectrometer (py-GC-MS), X-ray diffraction (XRD), and Raman spectroscopy can be used to analyze the pyrolysis process and product. Imaging methods such as scanning electron microscope (SEM) in combination with energy-dispersive X-ray spectroscopy (EDX) and transmission electron microscopy support the understanding of the nature of the carbon structure.

Raman spectroscopy has the ability to differentiate between graphitization and disordered carbon structures, corresponding to D1-band at around $1360\ cm^{-1}$ and G-band at around $1590\ cm^{-1}$, respectively.[38–46] As described by Jia et al.[40] the optimum carbon-based supercapacitor electrode should have a balance between disordered carbon to maintain porosity and ordered graphitized carbon to implement conductivity. XRD experiments are commonly used to characterize carbon structures. The average distance between the graphene layers can be determined from the spectrum using Bragg's law and the Scherrer equation. If the distance is greater than the reference value of 3.36 Å (0.336 nm), the disorder in the carbon increases and describes the turbostratic structure.[39–43,47,48] Doping with metals can enhance this formation,[38,39,48] and the relationship between increasing graphene interlayer spacing and the resulting increase in electrical conductivity is mentioned by Kokmat et al.[41] The surface structure (SSA and porosity) of electrode materials is generally analyzed by gas adsorption (e.g., Brunauer–Emmett–Teller (BET) method). Care must be taken to ensure that a disordered structure is formed in the carbon backbone rather than an ordered graphene structure. As a chaotic structure is the basis for the formation of pores, open and accessible pores are desirable for mass transfer. Pore formation takes place at pyrolysis temperatures between 700 and 900 °C.[49] Above 900 °C, the porous carbon structure changes to the formation of glassy carbon and the pore count is significantly reduced by repair mechanisms.[50] Glassy carbon is known for its stable and inert surface.[51,52] Coarse-pored structures can only be achieved by rapid pyrolysis.[53] After pyrolysis, an attached

activation step is essential to significantly increase the number of open pores. Depending on the process, different porosities can be obtained. Using a lithographic 3D printing process (digital light projection using liqiud crystal display (LCD), digital light processing [DLP]-LCD), highly accurate, isotropic, geometrically freely configurable 3D and self-supporting blanks with fine details, and a smooth surface from millimeter scale are produced. UV polymerization is the basis of additive 3D printing technology. A resin system specially adapted for the process based on acrylate is filled into the printer's resin tank. Layer by layer, specific areas are illuminated with UV light so-called "slices" and a 3D structure is gradually built up. The resulting 3D prints are characterized by a high spatial resolution (25–50 μm) and a smooth surface.

Narita et al.[42] used a DLP 3D printer and an acrylate-based resin patterned in a layer-by-layer manner by projected UV light to build the CAD-designed structure. The specialty about their process is the O_2 plasma etching of the 3D print before pyrolysis. The rough surface reduces the overpotential and increases the charge capacity. The use of electrodes is intended for battery storage, but supercapacitors are not considered.

Martinez et al.[54] used photopolymerization to develop 3D electrode structures exclusively for NMC batteries. Metal precursor salts are introduced into the resin and their influence on the manufacturing process is discussed.

Steldinger et al.[55] published stereolithography (SLA) 3D printing and photoinduced copolymerization of pentaerythritol tetraacrylate and divinylbenzene. Porogen as an additive of transport pores was part of the resin and consequently of the 3D printed and pyrolysis product. Additional CO_2 activation increases the BET porosity from 600 to $2200\ m^2\ g^{-1}$. The application of supercapacitor technology is often omitted.

In contrast, Wang et al.[43] produced porous electrodes specifically for supercapacitors and analyzed them regarding their electrochemical properties. A commercial resin was used as a photosensitive compound without further additives. After pyrolysis, activation with potassium hydroxide solution was carried out to achieve the microporosity required for supercapacitors. Carbon electrodes activated at 960 °C reveal a SSA of $101\ m^2\ g^{-1}$ (BET) and the pore size distribution features two peaks in the range of less than 2 and at 3.8 nm. The specific capacitance with a 2.5 mm-diameter electrode (S10 sample) at $1\ A\ cm^{-2}$ is around $23\ F\ g^{-1}$.

Here we present a new method for manufacturing electrodes for aqueous supercapacitors. Using masked SLA technique freestanding electrodes are produced with improved SSA and electrochemical properties compared to the mentioned literature. These electrodes do not contain metal foils and fluorinated binders, which we believe makes them cost effective and environmentally friendly alternatives to conventional ink-based and fluorinated binder-containing electrodes.

During this work we introduce a new formulation of a resin used for masked SLA print. To ensure porosity of electrodes, metal organic frameworks (MOF) were added as suggested by Dai et al.[56] Iron as metal was selected because of its cost effectiveness, its availability, and its noncritical character.[57]

In the course of this work, the production process of the electrodes is described, and the electrodes are characterized physiochemically and electrochemically for supercapacitor application.

2. Results and Discussion

2.1. Additive Manufacturing of the Electrodes

The masked SLA method was used to fabricate electrodes. The desired component is produced by polymerization using defined UV irradiation. The formulation of the resin was developed in house and contains MOF compound as an additive for creating porosity. The costs of the electrode are not affected by the use of MOFs. In the literature, prices for MOFs range between 7 and 60 € kg^{-1}.[58] The proportion of MOFs in the electrode is 2.89 wt%. In addition, Irgacure 819 was used as photoinitiator due to its low odor and low volatility. Furthermore, Irgacure 819 shows photosensitivity at longer wavelength (405 nm). It is of the utmost importance matching the light source and the activation of the photoinitiator for starting polymerization. Acrylates were selected as the oligomer and crosslinker because they react very sensitively to UV light exposure and promise short curing times ($\approx$2 s).[27] Moreover the oligomer is solvent resistant, cost-effective, and forms with the crosslinker a stable and hard polymer. We firmly believe that in the future the used resin materials can be replaced by more sustainable and bio-based materials like soybean oil-based components.[59] **Figure 1**a shows a structure produced using the masked SLA process. This structure is not electrically conductive after printing. For electrical conductivity, the material is subject to an attached pyrolysis step, resulting in an electrically conductive carbon structure (Figure 1b). For this purpose, the electrodes were pyrolyzed in ceramic tanks in the tube furnace.
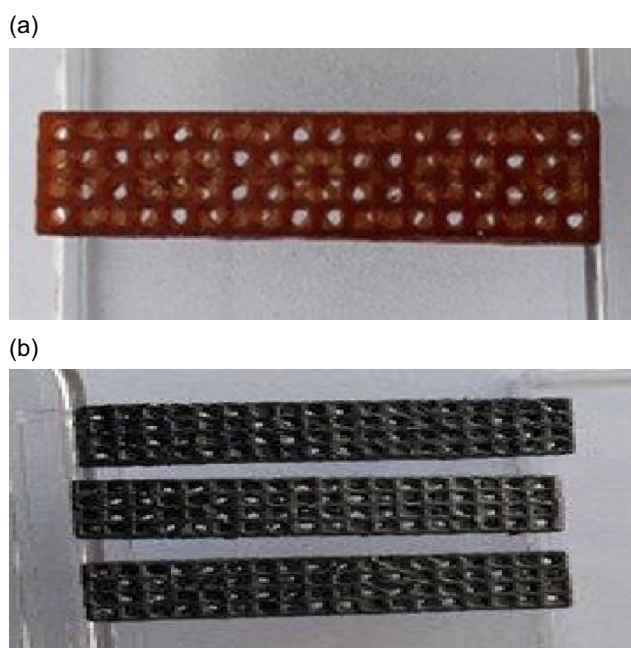
The electrodes obtained after pyrolysis are depicted in Figure 1b and show a color change to matt black, which indicates a change in the material structure. The shrinkage factor from the printed structure to the pyrolyzed and activated form is 1.6 and 1.7 respectively, resulting in mass losses of 79.5 and 82.5%. The pyrolysis process was analyzed using TGA and py-GC-MS. It was figured out that the mass loss was mainly due to the monomer, which is expected that polymerization was not fully completed during printing. Further investigations need to be carried out in the future to clarify this (see supporting material of TGA and py-GC-MS, Figure S2 and S3, Supporting Information).

In **Figure 2** two SEM pictures of pulverized electrode illustrate the porosity inside the carbon structure. Figure 2a presents the existing porosity of the printed electrode. The pores, in particular, are clearly recognizable in the red circle. In addition, in Figure 2b magnetite crystals are observed on the inside of the electrode, which were formed during pyrolysis. This is also confirmed by EDX experiments, which can be found in Figure S4, Supporting Information.

Figure 1. Additive manufactured electrodes: a) after printing and b) after pyrolysis.
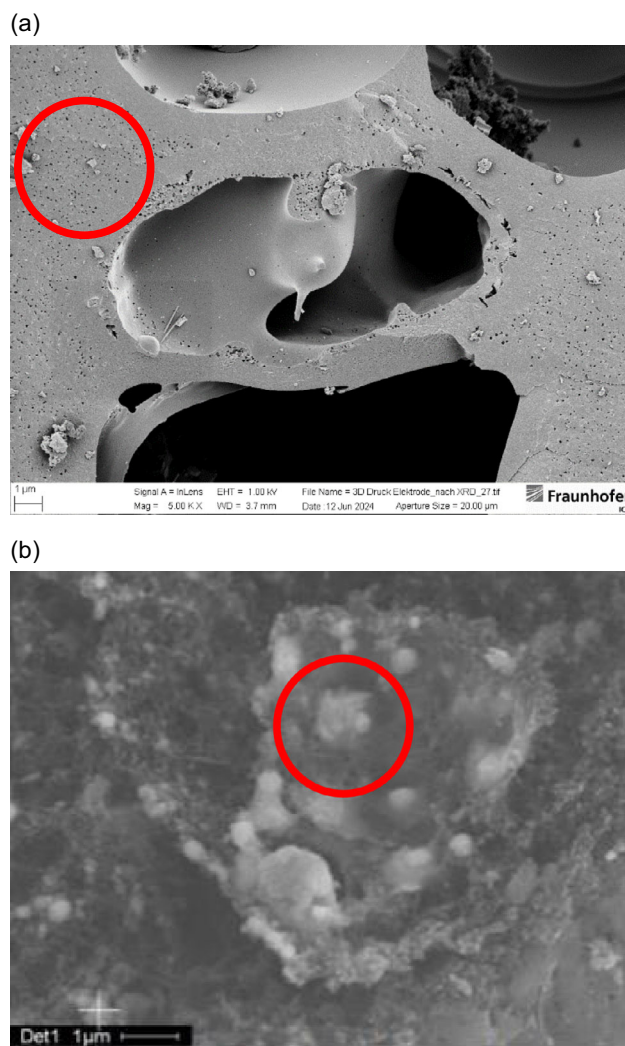

Figure 2. SEM pictures of carbon electrode: a) visible porosity of the electrode and b) magnetite crystals on top of the electrode surface.

In addition to the conductivity, which is essential for super-capacitor applications, the adjustment of the porosity was an important part of this work. Therefore, this article focuses on investigating and improving the pore size distribution of the printed electrodes. To gain knowledge of the porosity of the electrodes, a gas adsorption measurement of the electrodes was carried out after pyrolysis (**Figure 3**). The isotherm of the electrode clearly reveals the shape of a type 2 isotherm, which indicates a nonporous surface structure.[60] The SSA of the pyrolyzed electrode, which were also determined during this experiment, was not satisfactory for a suitable supercapacitor material with $8.9 \, m^2 \, g^{-1}$. The micropores required to store the energy were also not present in these structures.

However, the porous character changes significantly after activation of the electrode. The gas adsorption isotherm (**Figure 4**a) shows a microporous character (type 1 isotherm[60]). The additional activation step increased the SSA from 8 to $499 \, m^2 \, g^{-1}$. As these are initial activation tests, it can be assumed that significantly higher SSAs can be achieved through optimization efforts. For the pore size distribution (Figure 4b) of the activated carbon electrode a maximum in the microporous range between 0.4 and 0.8 nm is obtained. The SSA and the pore size distribution are in a range that is desired for electrodes in supercapacitors after the additional activation step.

In the Raman spectrum of **Figure 5**a, two peak bands are observed at 1360 and $1588 \, cm^{-1}$, which correspond to the D1-band and the G-band and are associated with disordered and ordered (graphitic) carbon, respectively.[41,42] The intensity (height) ratio (D/G) between them is 0.8 and can be considered as a balanced equilibrium between disordered and ordered carbon to obtain an optimal supercapacitor electrode.[40] Figure 5b contains a typical XRD diffractogram of activated carbon electrode as powder, which shows three broad peaks at $2\theta = 23.5°$, 43.7°, and 80°, respectively representing diffractions of 002, 100, and 110.[42] The presence of these broad peaks indicates that the carbon contains turbostratic graphene layers enabling high
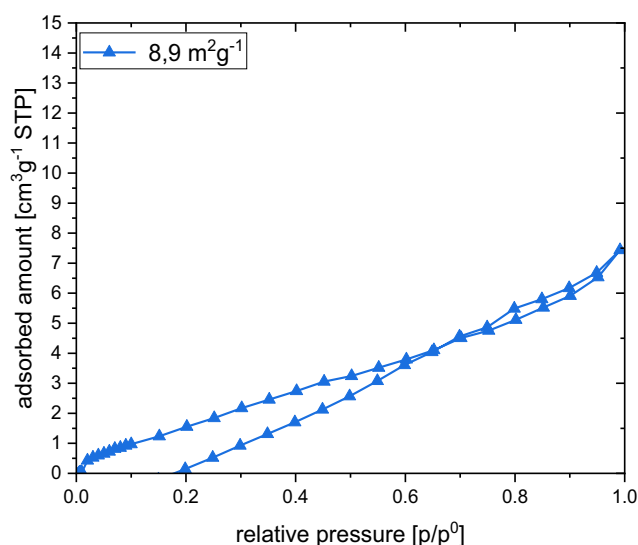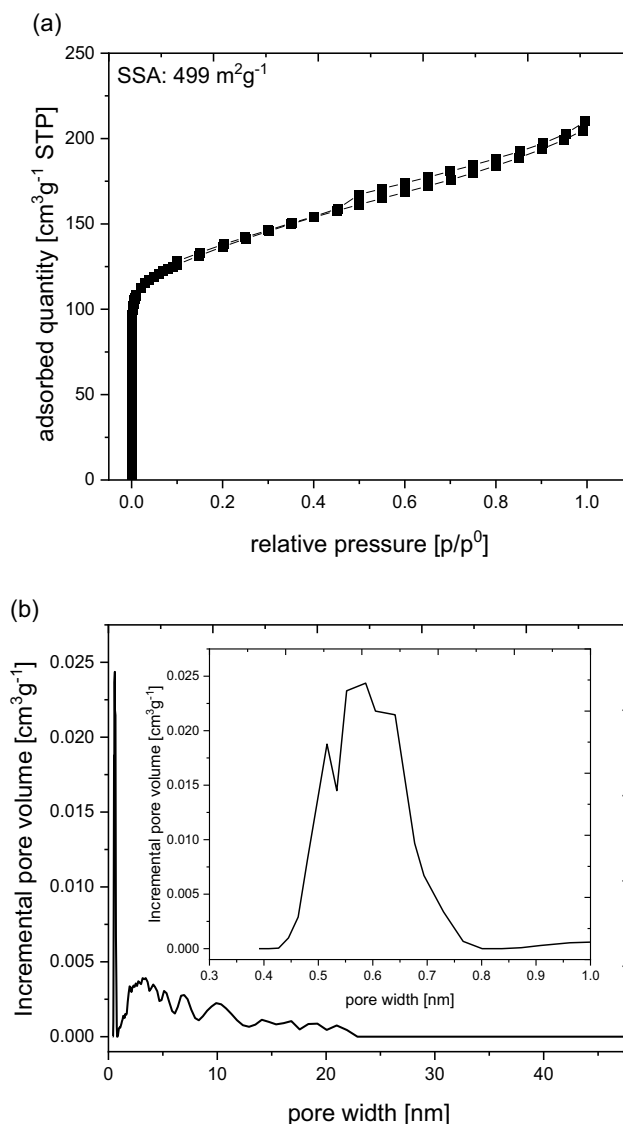
(a) SSA: 499 m^2g^{-1}

(b)

Figure 4. a) Gas adsorption isotherm and b) pore size distribution of additive manufactured electrode after activation.

electrical conductivity.[41,42] In XRD, the interlayer d002 is 0.392 nm (3915 Å) and is 16.67% bigger than that of crystalline graphite (3.36 Å).[40–42] Additionally, magnetite and iron can be identified caused by the addition of PCN-250 (Fe-MOF). The crystals of magnetite in the carbon structure are formed during pyrolysis and can be confirmed by SEM/EDX analysis (Figure 2 and Figure S4, Supporting Information).

2.2. Electrochemical Characterization

For electrochemical characterization, three-electrode and two-electrode arrangements were used. The electrolyte used was 6 M KOH, as the aim of this work was to demonstrate the feasibility of this idea of 3D-printed electrodes.

The cyclic voltammetry (CV) of a printed electrode in 6 M KOH in **Figure 6** shows that an electrochemical double layer is formed on the printed electrode. As desired, the CV forms a rectangular
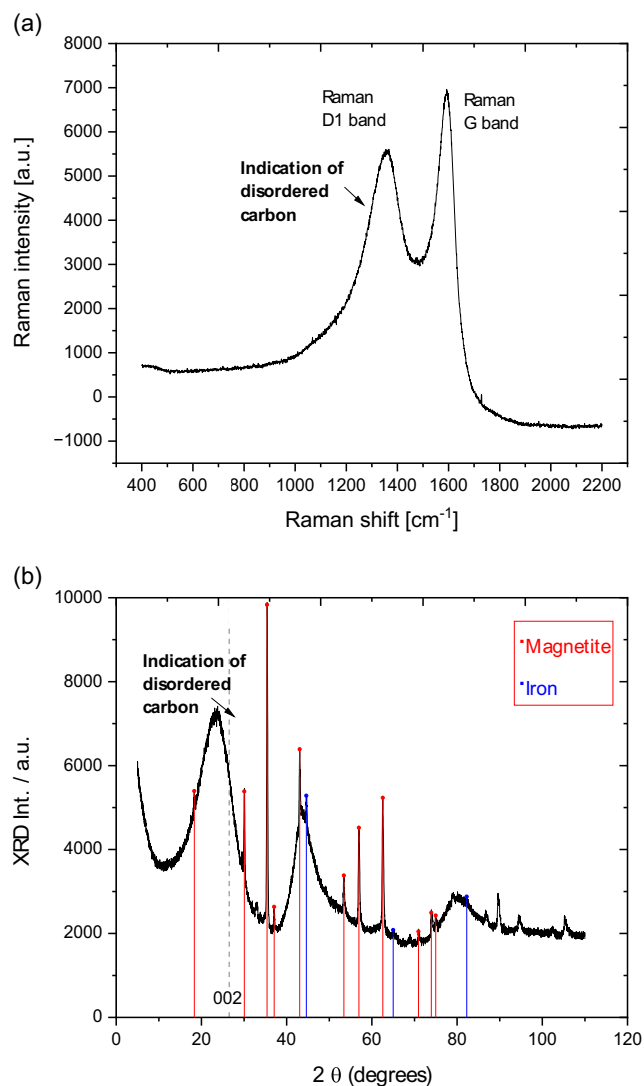
8,9 m^2g^{-1}

Figure 3. Adsorption isotherm of additively manufactured electrode after pyrolysis.

Batteries & Supercaps

Research Article
doi.org/10.1002/batt.202400455

Chemistry Europe
European Chemical
Societies Publishing

(a)

(b)

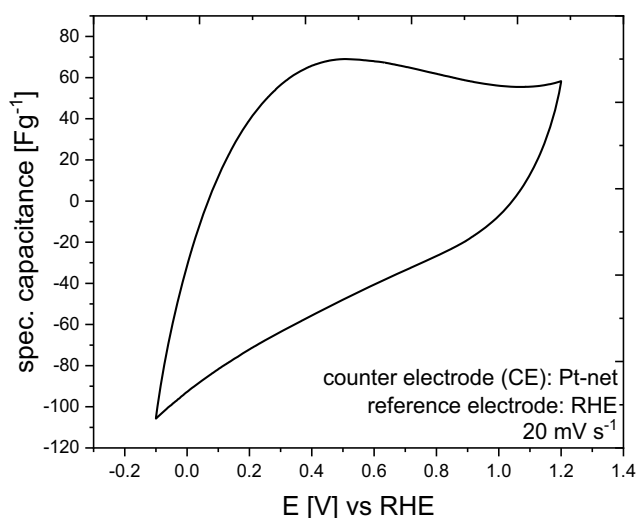**Figure 5.** a) Raman spectrum and b) XRD diffractogram spectrum of the activated carbon electrode.

Figure 6. CV of the printed electrode in the three-electrode arrangement in 6 M KOH; counter electrode: Pt-net; reference electrode: RHE at 20 mV s^{-1}.

shape. The slight distortion of the rectangle may result due to contact problems between the electrode and the potentiostat, as the printed electrodes are very brittle. Therefore, it was very important to be careful at electrical contacting to avoid damage of the electrodes. The electrode enables an electrochemical stability window (ESW) of 1.2 V in 6 M KOH, which is comparable to the conventionally produced electrodes. The galvanostatic charge/discharge curves (**Figure 7**a) form symmetrical triangles and result in a sufficiently high specific capacitance of 74 F g^{-1} up to a discharge current of 2 A g^{-1}. The drop in capacitance at higher currents can be explained by the absence of mesopores (see Figure 4b).

These are required to enable rapid ion transport at high currents. However, this type of pore is missing in the printed electrodes and would have to be integrated into the manufacturing process in further research work. Figure 7b shows that the printed electrodes have sufficient electrical conductivity confirmed by the almost perfect rectangular shape of CVs at higher scan rates.
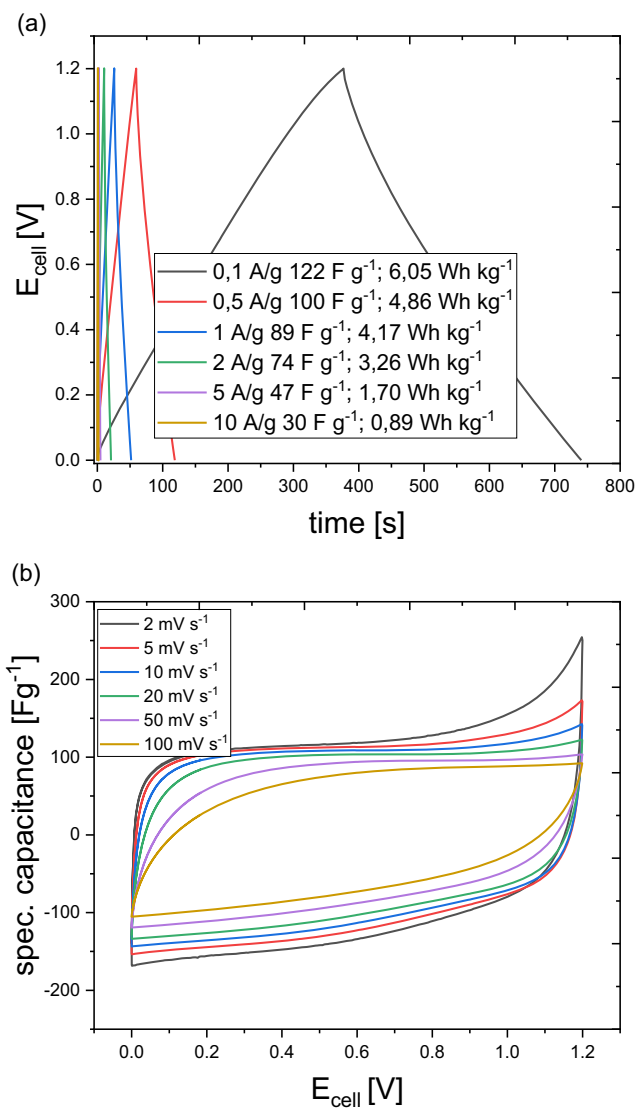
(a)

(b)

Figure 7. a) Galvanostatic charge/discharge curves at different specific current densities and b) CV experiments of printed electrodes in supercapacitor cells at different scan rates (right) in 6 M KOH.

Batteries & Supercaps

Research Article
doi.org/10.1002/batt.202400455

Chemistry Europe
European Chemical
Societies Publishing

This is evidence of good conductivity and low resistance of the entire system, but also of the electrodes used. It can also be extracted from the CVs that the area under the CV becomes smaller at higher scan rates, which corresponds to a smaller specific capacitance of the capacitor. However, no distortion of the CV can be seen even at $100\,mV\,s^{-1}$.

Finally, the printed electrodes were compared with the conventional electrodes. **Figure 8**a presents the Nyquist plots of two supercapacitor cells with differently produced electrodes. The shape of the Nyquist plots is similar, one semicircle at high frequency, a straight line with a slope of 45° line at high–middle frequency, and a nearly vertical line at low-frequency values.
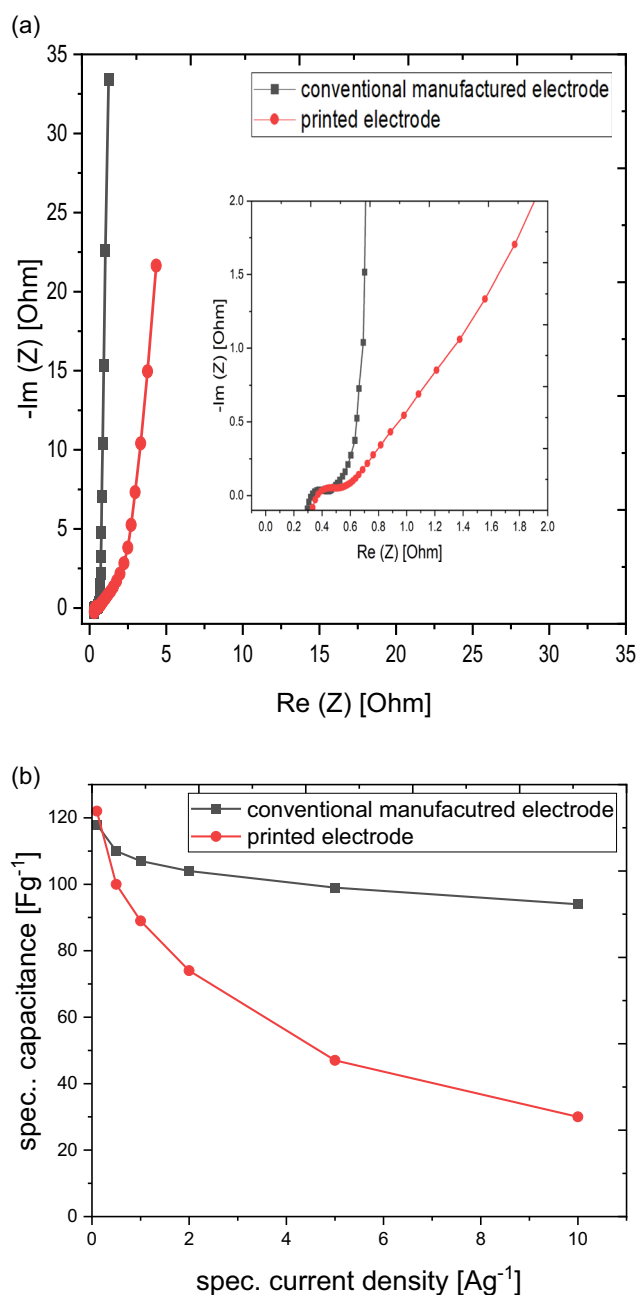
The ESR and thus the internal resistance of the cell in both supercapacitors is similar at 0.3 Ω, which speaks in favor of the suitability of the printed electrodes. As in the previous experiments observed, one difference between the two types of electrodes was found in the diffusion. After the appearance of the semicircle the graph of the conventional manufactured electrode shows a short 45° line turning immediately into a 90° line which is perpendicular to the y-axis. This indicates a high accessibility of the ions to the electrode and a good diffusion within the electrode.[61] Whereas for the printed electrode the 45° line is more pronounced displaying hindered diffusion of ions within the electrode.[62] The reason for this has already been explained with the different pore structure (missing mesopores in printed electrodes). This also applies to the comparison of the specific capacitances in Figure 8b of the two differently produced electrodes. Here it can be seen that supercapacitors with both printed and conventional electrodes have a similarly high spec. capacitance of $120\,F\,g^{-1}$ at low currents. However, at higher currents, the supercapacitor with the printed electrodes degrades significantly due to the lack of mesopores. This needs to be improved in the future, as well as the fragility of the material. What is remarkable, however, is that the printed electrodes work in principle and can make a significant contribution to using more environmentally friendly materials in energy storage systems.

3. Conclusion

In this work we present a new approach for the fabrication of electrodes in supercapacitors. Additive manufacturing is used to produce binder-free electrodes that do not require metal foils. The electrodes produced in this way are subjected to thermal pyrolysis and activation to obtain porous carbon electrodes. The electrodes produced have a microporous surface structure and SSA of $499\,m^2\,g^{-1}$. These surface properties are suitable for use in supercapacitors. The results of the electrochemical characterization of both the single electrode and a complete supercapacitor cell reveal that the requirements for applications in supercapacitors are met. The cyclic voltammograms indicate capacitive behavior and high electrical conductivity of the electrodes. Galvanostatic cycling experiments clearly display that the obtained spec. capacitances of supercapacitors with printed electrodes are comparable with conventionally manufactured electrodes, especially at low current densities. At higher current densities, the capacitance of the printed electrodes drops slightly due to the lack of mesopores. These need to be introduced in future experiments. Nevertheless, it could be shown that a critical raw material- and binder-free supercapacitor can be produced.

4. Experimental Section

Electrode Preparation: Conventional Electrodes

Conventional carbon electrodes were prepared as follows. 10 wt% of polytetrafluoroethylene (PTFE) dispersion (60 wt% in H_2O, Sigma

Figure 8. Comparison of conventional electrodes with printed electrodes: a) Nyquist plot and b) spec. capacitances in 6 M KOH.

Batteries & Supercaps

Research Article
doi.org/10.1002/batt.202400455

**Chemistry
Europe**

European Chemical
Societies Publishing

Aldrich) was dispersed in an 3:1 vol:vol ethanol/H_2O mixture and stirred for 30 min. 10 wt% Vulcan XC72R (Cabot Corporation) was added as a conducting agent and the mixture was stirred for another 30 min. 80 wt% activated carbon (DLC 30 from Norit) was added to the dispersion and stirred for another 60 min. Then the prepared slurry was coated onto a nickel foam by doctor blade method. The coated nickel foam was dried overnight in a vacuum oven at 80 °C. Subsequently the dried electrode was pressed at 50 kN. The area of the manufactured electrode was 0.785 cm². The thickness of the electrode was 420 μm with a mass loading between 10 and 13 mg cm⁻².

Electrode Preparation: Printed Electrodes

A liquid acrylate resin consisting of an oligomer (bisphenol A glycerolate from Merck), photoinitiator (bis(2,4,6-trimethylbenzoyl)-phenylphosphine oxide from Irgacure 819), crosslinker (di-[1,1,1, tris(hydroxymethyl)propane]-tetraacrylate from Merck), and an additive (Fe MOF PCN-250 from CD Bioparticles) was used to produce the printed electrodes.[63] For the resin, the photoinitiator (0.1 g) was completely dissolved in acetonitrile (1.0 g). The crosslinker (4.2 g), the oligomer (12.5 g) and the DMSO (4.0 g) were added, slightly heated, and homogenized using a stirrer. The additive was implemented as the last component and stirred for 2 h. 3D printing was carried out on the same day using the Photon S from Anycubic. The resin was in a vat with a transparent base (fluorinated ethylene propylene [FEP] film with a thickness of 150 μm). This vat was placed on a screen that emitted the UV light required to cure the resin. The structure was built on the surface of a building platform. This platform can be moved along the z-axis (platform raise velocity 70 mm min⁻¹ platform raise height 5 mm) and was immersed in the liquid resin up to a certain distance above the screen (platform raise height 5 mm). This determined the layer thickness of the structure. By illuminating (wavelength for photopolymerization 405 nm) locally defined areas, the resin hardened on the surface of the building platform and thus built up the structure "upside down" and layer by layer. The polymerization of the 3D print was carried out with a layer thickness of 100 μm with an exposure duration of 70 s. After successful printing of the object (thickness of 0.5 mm), pyrolysis took place in ceramic tanks. For this purpose, the tube furnace was heated to 420 °C at 10 °C min⁻¹. This temperature was maintained for 2 h. This was followed by a further temperature ramp with 10 °C min⁻¹ to 750 °C. Temperature was held for a further 12 h. The atmosphere was under nitrogen, which was added at a flow rate of 0.5 L min⁻¹. After pyrolysis, the samples were activated to open the pores of the electrodes. For this purpose, the samples were heated to 880 °C at 10 °C min⁻¹ in a CO_2 atmosphere and kept at this temperature for 1.5 h. The printed carbon electrodes were disks with an area of 0.785 cm² and a thickness of 0.2 mm. The as-prepared electrodes were used for electrochemical measurements without further processing.

Structural Analysis: Gas Adsorption Measurements

For gas adsorption analysis, carbon material was heated at 300 °C for 15 h under vacuum to degas the contaminants physically adsorbed on the surface. The SSA was calculated from nitrogen adsorption/desorption isotherm experiments recorded at 77 K (3Flex, Micromeritics).

Structural Analysis: SEM

SEM images of selected samples were taken using the Zeiss EVO MA10 SEM. The acceleration voltage was 16 kV.

Structural Analysis: EDX

In addition, EDX were recorded in the Energetic Materials Department using an Oxfords Instruments device with an X-Max 80 mm².

Structural Analysis: Raman Measurements

Raman spectra were acquired from HORIBA Jobin Yvon with the model RA_LabHR S/N L HR 2/594. The excitation of the laser was 473 nm with following settings: no usage of filter, 500 μm hole, and 100 μm slice.

Structural Analysis: XRD Measurements

The carbon electrode was ground into powder using a mortar and pestle to analyze the crystal structure using XRD analysis from Bruker AXS (D8 Advance DaVinci). Copper radiation was used at 40 kV and 40 mA. Following parameters were used: variable divergence aperture (10 mm); 2.5° axial setter, scattered beam aperture in automatic mode, sample rotation $= 10.0$ rpm, LynxEye_XE_T silicon strip detector, aperture angle $= 2.94$°; 2.5° axial setter, scan range $5.0–110.0$°2θ, step size $= 0.02$°2θ; measurement time per step $= 1.5$ sec. The L_c parameter was calculated using Scherrer's equation with the values of K $= 0.94$.

Structural Analysis: TGA

The thermogravimetric analyses of the 3D-printed electrodes were carried out with a thermogravimetric MS from Netzsch (TG 209 F1 Iris ASC (without QMS 403 C Aeolos)). Netzsch's Proteus software was used to control and analyze the measurement data.

The gases emitted at certain temperatures were transferred to the measuring cell of the MS using a thermostatted transfer (heated to 280 °C). The data from the MS was analyzed using the Quadstar software from Bruker Instruments. 9 mg of the sample was weighed into an aluminum oxide crucible and placed in the thermobalance. This was followed by the actual measurement program. The sample was heated over a temperature range of 25–700 °C under nitrogen at a heating rate of 2 K min⁻¹. The flow rate of the nitrogen was 40 mL min⁻¹.

Electrochemical Characterization

All electrochemical experiments were performed at room temperature. The ESW of the investigated electrolyte and printed electrode system were determined using a three-electrode setup equipped with a platinum net as the counter electrode and a reversible hydrogen electrode (RHE, Gaskatel) as the reference electrode in a beaker. The used electrolyte was 6 M KOH with a potential range of 1.2 V.

Symmetric two-electrode (soaking time 12 h) cells were used for electrochemical characterization of a full-symmetric supercapacitor cell. The measuring cells consisted of a glass cell and two stainless steel plungers. The electrodes, which were separated by a separator wet with electrolyte, were placed between the two stainless steel stamps. The cells were fixed with screw caps and contacted with the potentiostat via the stainless steel stamps (Figure S1, Supporting Information). The electrodes were immersed in the electrolyte for 12 h. The separator served as a poly-olefine-based membrane (Freudenberg) soaked with the electrolyte. CV was applied for observing the electrochemical performance at different scan rates (2, 5, 10, 20, 50, and 100 mV s⁻¹) and galvanostatic charge and discharge experiments (0.1, 0.5, 1.0, 2.0, 5.0, 10.0 A g⁻¹) using a VMP3 multi-channel potentiostat (Biologic). The gravimetric capacitance of

Batteries & Supercaps

Research Article
doi.org/10.1002/batt.202400455

Chemistry Europe
European Chemical
Societies Publishing

one electrode C_e in $\mathrm{F\,g^{-1}}$ was calculated by Equation (1) from the galvanostatic discharge curve.[12]

$$C_e = \frac{2 * I * \Delta t}{\Delta V * m} \tag{1}$$

where I is the current [A], t the discharge time [s], ΔV the IR drop-corrected cell voltage [V], and m [g] the active mass in one electrode. The energy density of a full supercapacitor device was calculated according to Equation (2)[64]

$$E = \frac{1}{2} * \frac{C_e}{4} * \Delta V^2 * \frac{1}{3.6} \tag{2}$$

C_e is specific capacitance and ΔV represents the IR drop-corrected operating voltage.

Impedance experiments were conducted at open-circuit potential in the range of 10 mHz–100 kHz with an amplitude of 10 mV.

Acknowledgements

Conflict of Interest

The authors declare no conflict of interest.

Data Availability Statement

The data that support the findings of this study are available from the corresponding author upon reasonable request.

[1] A. B. Gallo, J. R. Simões-Moreira, H. Costa, M. M. Santos, E. Moutinho dos Santos, *Renewable Sustainable Energy Rev.* **2016**, *65*, 800.
[2] A. Kalair, N. Abas, M. S. Saleem, A. R. Kalair, N. Khan, *Energy Storage* **2021**, *3*, e135.
[3] E. Sayed, A. Olabi, A. Alami, A. Radwan, A. Mdallal, A. Rezk, M. Abdelkareem, *Energies* **2023**, *16*, 1415.
[4] A. Cortez, N. Nguyen, R. K. Jones, *2021 IEEE 48th Photovoltaic Specialists Conference (PVSC)*, IEEE, Fort Lauderdale, Fl, USA **2021**, pp. 206.
[5] D. N. Buckley, C. O'Dwyer, N. Quill, R. P. Lynch, *Energy Storage Options And Their Environmental Impact* (Eds: R. E. Hester, R. M. Harrison), The Royal Society of Chemistry, Cambridge, UK **2018**, pp. 115–149.
[6] S. Sarmah, Lakhanlal, B. K. Kakati, D. Deka, *WIREs Energy Environ.* **2023**, *12*, e461.
[7] Y. Zhao, O. Pohl, A. I. Bhatt, G. E. Collis, P. J. Mahon, T. Rüther, A. F. Hollenkamp, *Sustainable Chem.* **2021**, *2*, 167.
[8] C. M. Costa, J. C. Barbosa, R. Gonçalves, H. Castro, F. J. Del Campo, S. Lanceros-Méndez, *Energy Storage Mater.* **2021**, *37*, 433.
[9] B. E. Lebrouhi, S. Baghi, B. Lamrani, E. Schall, T. Kousksou, *J. Energy Storage* **2022**, *55*, 105471.
[10] W. Zuo, R. Li, C. Zhou, Y. Li, J. Xia, J. Liu, *Adv. Sci.* **2017**, *4*, 1600539.
[11] Q. Gou, S. Zhao, J. Wang, M. Li, J. Xue, *Nano Micro Lett.* **2020**, *12*, 98.
[12] T. Cetinkaya, R. A. Dryfe, *J. Power Sources* **2018**, *408*, 91.
[13] K. Gajewska, A. Moyseowicz, D. Minta, G. Gryglewicz, *J. Mater. Sci.* **2023**, *58*, 1721.
[14] N. Böckenfeld, S. S. Jeong, M. Winter, S. Passerini, A. Balducci, *J. Power Sources* **2013**, *221*, 14.
[15] S. S. Jeong, N. Böckenfeld, A. Balducci, M. Winter, S. Passerini, *J. Power Sources* **2012**, *199*, 331.
[16] N. T. Baltes, J. Heumann, P. M. Rabenecker, J. Tübke, *Chem. Eng. J.* **2023**, *476*, 146517.
[17] M. Aslan, D. Weingarth, N. Jäckel, J. S. Atchison, I. Grobelsek, V. Presser, *J. Power Sources* **2014**, *266*, 374.
[18] S. Paul, K. S. Choi, D. J. Lee, P. Sudhagar, Y. S. Kang, *Electrochim. Acta* **2012**, *78*, 649.
[19] B. K. Saikia, S. M. Benoy, M. Bora, J. Tamuly, M. Pandey, D. Bhattacharya, *Fuel* **2020**, *282*, 118796.
[20] N. Blomquist, T. Wells, B. Andres, J. Bäckström, S. Forsberg, H. Olin, *Sci. Rep.* **2017**, *7*, 39836.
[21] G. Jiang, S. J. Pickering, *Waste Manage.* **2016**, *48*, 465.
[22] Y.-Z. Zhang, Y. Wang, T. Cheng, W.-Y. Lai, H. Pang, W. Huang, *Chem. Soc. Rev.* **2015**, *44*, 5181.
[23] D. M. Soares, Z. Ren, S. B. Mujib, S. Mukherjee, C. G. Martins Real, M. Anstine, H. Zanin, G. Singh, *Adv. Energy Sustainability Res.* **2021**, *2*, 2000111.
[24] A. De, B. Ramasubramanian, S. Ramakrishna, V. Chellappan, *Adv. Mater. Technol.* **2023**, *9*, 2301439.
[25] G. F. Hawes, S. Rehman, Y. Rangom, M. A. Pope, *Int. Mater. Rev.* **2023**, *68*, 323.
[26] R. Amin, S. Knowlton, A. Hart, B. Yenilmez, F. Ghaderinezhad, S. Katebifar, M. Messina, A. Khademhosseini, S. Tasoglu, *Biofabrication* **2016**, *8*, 22001.
[27] D. Bird, E. Caravaca, J. Laquidara, K. Luhmann, N. M. Ravindra, *The Minerals, Metals & Materials Series*, Springer International Publishing, Cham **2019**, pp. 1575–1587.
[28] B. Cardenas-Benitez, C. Eschenbaum, D. Mager, J. G. Korvink, M. J. Madou, U. Lemmer, I. de Leon, S. O. Martinez-Chapa, *Microsyst. Nanoeng.* **2019**, *5*, 38.
[29] X. Wang, X. Lu, B. Liu, D. Chen, Y. Tong, G. Shen, *Adv. Mater.* **2014**, *26*, 4763.
[30] A. G. Pandolfo, A. F. Hollenkamp, *J. Power Sources* **2006**, *157*, 11.
[31] Z. Zhai, L. Zhang, T. Du, B. Ren, Y. Xu, S. Wang, J. Miao, Z. Liu, *Mater. Des.* **2022**, *221*, 111017.
[32] R. Mendoza, J. Oliva, V. Rodriguez-Gonzalez, *Int. J. Energy Res.* **2022**, *46*, 6989.
[33] J. Huang, Y. Liang, H. Hu, S. Liu, Y. Cai, H. Dong, M. Zheng, Y. Xiao, Y. Liu, *J. Mater. Chem. A* **2017**, *5*, 24775.
[34] Y. Wu, C. Cao, *Sci. China Mater.* **2018**, *61*, 1517.
[35] P. Forouzandeh, V. Kumaravel, S. C. Pillai, *Catalysts* **2020**, *10*, 969.
[36] A. Platek-Mielczarek, J. Conder, K. Fic, C. M. Ghimbeu, *J. Power Sources* **2022**, *542*, 231714.
[37] Z. Q. Chen, Y. F. Chen, H. B. Liu, *AMM* **2013**, *422*, 24.
[38] L. G. Cançado, K. Takai, T. Enoki, M. Endo, Y. A. Kim, H. Mizusaki, A. Jorio, L. N. Coelho, R. Magalhães-Paniago, M. A. Pimenta, *Appl. Phys. Lett.* **2006**, *88*, 163106.
[39] N. K. Chaudhari, S. Chaudhari, J.-S. Yu, *ChemSusChem* **2014**, *7*, 3102.
[40] D. Jia, X. Yu, H. Tan, X. Li, F. Han, L. Li, H. Liu, *J. Mater. Chem. A* **2017**, *5*, 1516.
[41] P. Kokmat, P. Surinlert, A. Ruammaitree, *ACS Omega* **2023**, *8*, 4010.
[42] K. Narita, M. A. Citrin, H. Yang, X. Xia, J. R. Greer, *Adv. Energy Mater.* **2021**, *11*, 2002637.
[43] P. Wang, H. Zhang, H. Wang, D. Li, J. Xuan, L. Zhang, *Adv. Mater. Technol.* **2020**, *5*, 2070034.
[44] A. C. Ferrari, J. Robertson, *Phys. Rev. B* **2000**, *61*, 14095.
[45] T.-H. Ko, W.-S. Kuo, Y.-H. Chang, *Polym. Compos.* **2000**, *21*, 745.
[46] K. Ishimaru, T. Hata, P. Bronsveld, T. Nishizawa, Y. Imamura, *J. Wood Sci.* **2007**, *53*, 442.
[47] Z. Q. Li, C. J. Lu, Z. P. Xia, Y. Zhou, Z. Luo, *Carbon* **2007**, *45*, 1686.
[48] K. Inomata, Y. Otake, *J. Mater. Sci.* **2011**, *46*, 2194.
[49] P. Ouzilleau, A. E. Gheribi, P. Chartrand, G. Soucy, M. Monthioux, *Carbon* **2019**, *149*, 419.
[50] P. J. F. Harris, *Crit. Rev. Solid State Mater. Sci.* **2005**, *30*, 235.
[51] S. Sharma, *Materials* **2018**, *11*, 1.
[52] L. d. S. Vieira, *Carbon* **2022**, *186*, 282.
[53] S. Sharma, R. Kamath, M. Madou, *J. Anal. Appl. Pyrolysis* **2014**, *108*, 12.
[54] A. C. Martinez, A. Maurel, A. P. Aranzola, S. Grugeon, S. Panier, L. Dupont, J. A. Hernandez-Viezcas, B. Mummareddy, B. L. Armstrong, P. Cortes, S. T. Sreenivasan, E. MacDonald, *Sci. Rep.* **2022**, *12*, 19010.
[55] H. Steldinger, A. Esposito, K. Brunnengräber, J. Gläsel, B. J. M. Etzold, *Adv. Sci.* **2019**, *6*, 1901340.
[56] Y. Dai, C. Liu, Y. Bai, Q. Kong, H. Pang, *Nanotechnol. Rev.* **2022**, *11*, 1005.
[57] P. Du, R. Eisenberg, *Energy Environ. Sci.* **2012**, *5*, 6012.

Batteries & Supercaps

Research Article
doi.org/10.1002/batt.202400455

Chemistry
Europe

European Chemical
Societies Publishing

[58] D. DeSantis, J. A. Mason, B. D. James, C. Houchins, J. R. Long, M. Veenstra, *Energy Fuels* **2017**, *31*, 2024.

[59] J. Guit, M. B. Tavares, J. Hul, C. Ye, K. Loos, J. Jager, R. Folkersma, V. S. Voet, *ACS Appl. Polym. Mater.* **2020**, *2*, 949.

[60] P. A. Webb, C. Orr, *Analytical Methods in Fine Particle Technology*, Micrometrics Instrument Corporation, Norcross, GA, USA **1997**.

[61] T. S. Mathis, N. Kurra, X. Wang, D. Pinto, P. Simon, Y. Gogotsi, *Adv. Energy Mater.* **2019**, *9*, 192007.

[62] K. L. van Aken, J. K. McDonough, S. Li, G. Feng, S. M. Chathoth, E. Mamontov, P. F. Fulvio, P. T. Cummings, S. Dai, Y. Gogotsi, *J. Phys. Condens. Matter* **2014**, *26*, 284104.

[63] S. Yuan, X. Sun, J. Pang, C. Lollar, J.-S. Qin, Z. Perry, E. Joseph, X. Wang, Y. Fang, M. Bosch, D. Sun, D. Liu, H. C. Zhou, *Joule* **2017**, *1*, 806.

[64] M. Wahid, G. Parte, R. Fernandes, D. Kothari, S. Ogale, *RSC Adv.* **2015**, *5*, 51382.